Cellular/Molecular

Lunatic Fringe-GFP Marks Lamina-Specific Astrocytes That Regulate Sensory Processing

Ekin Su Akdemir,[1,2] Junsung Woo,[2] Navish A. Bosquez Huerta,[1,2] Brittney Lozzi,[2] Andrew K. Groves,[1,3,4] Akdes Serin Harmanci,[5] and Benjamin Deneen[1,2,3,5]

[1]Program in Developmental Biology, Baylor College of Medicine, Houston, Texas 77030, [2]Center for Cell and Gene Therapy, Baylor College of Medicine, Houston, Texas 77030, [3]Department of Neuroscience, Baylor College of Medicine, Houston, Texas 77030, [4]Department of Human and Molecular Genetics, Baylor College of Medicine, Houston, Texas 77030, and [5]Department of Neurosurgery, Baylor College of Medicine, Houston, Texas 77030

Astrocytes are the most abundant glial cell in the brain and perform a wide range of tasks that support neuronal function and circuit activities. There is emerging evidence that astrocytes exhibit molecular and cellular heterogeneity; however, whether distinct subpopulations perform these diverse roles remains poorly defined. Here we show that the Lunatic Fringe-GFP (Lfng-GFP) bacteria artificial chromosome mouse line from both sexes specifically labels astrocyte populations within lamina III and IV of the dorsal spinal cord. Transcriptional profiling of Lfng-GFP$^+$ astrocytes revealed unique molecular profiles, featuring an enriched expression of Notch- and Wnt- pathway components. Leveraging CRE-DOG viral tools, we ablated Lfng-GFP$^+$ astrocytes, which decreased neuronal activity in lamina III and IV and impaired mechanosensation associated with light touch. Together, our findings identify Lfng-GFP$^+$ astrocytes as a unique subpopulation that occupies a distinct anatomic location in the spinal cord and directly contributes to neuronal function and sensory responses.

Key words: **astrocyte; circuit activities; glia; sensory processing; spinal cord**

Significance Statement

Astrocytes are the most abundant glial cell in the CNS, and their interactions with neurons are essential for brain function. However, understanding the functional diversity of astrocytes has been hindered because of the lack of reporters that mark subpopulations and genetic tools for accessing them. We discovered that the Lfng-GFP reporter mouse labels a laminae-specific subpopulation of astrocytes in the dorsal spinal cord and that ablation of these astrocytes reduces glutamatergic synapses. Further analysis revealed that these astrocytes have a role in maintaining sensory-processing circuity related to light touch.

Introduction

Astrocytes are the most abundant type of glial cell in the CNS and have long been recognized as essential for CNS development and function (Allen and Barres, 2009; Molofsky and Deneen, 2015). Astrocytes have diverse physiological roles in neural development and CNS functioning, including forming the blood–brain barrier, promoting synaptogenesis, participating in neurotransmission, providing metabolic support of neurons, and secreting molecules that modulate neuronal activity (Khakh and Sofroniew, 2015; Allen and Eroglu, 2017; Khakh and Deneen, 2019). Despite these broad physiological functions, it has been challenging to decipher whether distinct subpopulations of astrocytes execute these diverse roles (Khakh and Sofroniew, 2015; Allen and Eroglu, 2017; Khakh and Deneen, 2019).

For over 100 years, it has been appreciated that the brain is composed of a wide array of morphologically diverse glial populations present throughout the neural axis (Ramon y Cajal, 1897). While astrocytes have been classified into the following two broad morphologic groups: protoplasmic or fibrous, unlike neurons, they are electrically silent and therefore difficult to characterize by electrophysiology. However, more recent studies in developmental systems have demonstrated new ways to categorize astrocytes (Ben Haim and Rowitch, 2017). Combinatorial expression of patterning-associated transcription factors revealed astrocyte subpopulations with unique expression profiles in ventral spinal cord white matter (Hochstim et al., 2008). Lineage

Received July 6, 2021; revised Nov. 22, 2021; accepted Nov. 28, 2021.

Author contributions: E.S.A. and B.D. designed research; E.S.A., J.W., N.A.B.H., and B.L. performed research; A.K.G. contributed unpublished reagents/analytic tools; E.S.A., A.S.H., and B.D. analyzed data; E.S.A. and B.D. wrote the paper.

This work was supported by grants from the National Institutes of Health (NIH; NS-071153 and AG-071687 to BD; DC-014832 to A.K.G.) and by the Cytometry and Cell Sorting Core at Baylor College of Medicine with funding from the CPRIT Core Facility Support Award (Grant CPRIT-RP180672), the NIH (Grants CA-125123 and RR-024574), and the assistance of Joel M. Sederstrom. We thank Surabi Veeraragaven for assistance with the behavior assays, the Optogenetics and Viral Vectors Core at the Jan and Dan Duncan Neurological Research Institute, and Dinghui Yu of the Microscopy Core Jan and Dan Duncan Neurological Research Institute for assistance on confocal imaging.

The authors declare no competing financial interests.

Correspondence should be addressed to Benjamin Deneen at deneen@bcm.edu.

https://doi.org/10.1523/JNEUROSCI.1392-21.2021

tracing of these patterned spinal cord domains confirmed the presence of astrocyte subpopulations along the dorsal/ventral axis (Tsai et al., 2012). In addition to studies in the developing spinal cord, a series of recent studies has also identified molecular diversity in the adult brain (Khakh and Deneen, 2019). These include identifying molecular diversity across distinct brain regions (i.e., hippocampus and striatum) and unique interactions with region-specific neuronal populations (Morel et al., 2017). Local diversity of astrocytes within brain regions also was demonstrated using FACS-based and single-cell profiling approaches (John Lin et al., 2017; Batiuk et al., 2020; Bayraktar et al., 2020). Nevertheless, how molecularly distinct astrocyte populations differentially influence circuit function remains poorly defined.

Synaptic inputs from peripheral sensory neurons into the CNS occur in the dorsal horn of the spinal cord, which is densely populated by astrocytes. Recent studies found that dorsal astrocytes exhibit unique patterns of marker gene expression and laminar-specific coupling speed (Kronschläger et al., 2021). Accordingly, astrocytes have been implicated in sensory processing, where the inhibition of astrocyte proliferation reduced injury-induced tactile allodynia (Tsuda et al., 2011). In contrast, the injection of reactive astrocytes with cytokines into the spinal cord increased mechanical allodynia (Gao et al., 2010). In addition to inflammation pathways, direct optogenetic and chemogenetic stimulation of dorsal astrocytes induced mechanical hypersensitivity through ATP and D-serine, respectively (Nam et al., 2016; Kohro et al., 2020). These distinct mechanisms suggest that different subsets of astrocytes contribute to sensory processing, highlighting the need to develop new genetic tools to trace and manipulate them (Tsuda et al., 2011; Ji et al., 2019).

In this study, we found that the Lunatic Fringe-GFP (Lfng-GFP) bacteria artificial chromosome (BAC) mouse line specifically labels a subpopulation of astrocytes in the dorsal horn of the spinal cord. Lunatic Fringe (*Lfng*) is a glycosyltransferase enzyme that modifies Notch receptor and plays a key role in Notch signaling (LeBon et al., 2014). Lfng-GFP$^+$ astrocytes localize within lamina III and IV and are endowed with unique molecular profiles compared with other spinal cord astrocytes. We leveraged viral tools to genetically ablate this subpopulation, which impaired both neuronal activity in lamina III and IV and sensory processing of touch. Together, our findings indicate that Lfng-GFP$^+$ astrocytes are a unique subpopulation that occupies the dorsal spinal cord and contributes to neuronal function and associated tactile responses.

Materials and Methods

Animals. All experimental animals were treated according to the US Department of Health and Human Services and Baylor College of Medicine Institutional Animal Care and Use Committee guidelines. All mice were housed with food and water available *ad libitum* in a 12 h light/dark environment. Both male and female mice were used for all experiments, and mice were randomly allocated to experimental groups. For the *ex vivo* and *in vivo* experiments, adult mice, 8–12 weeks of age, were used unless otherwise described. Both male and female Lfng-GFP and Aldh1l1-GFP mice were used and maintained on the C57BL/6J background. The Lfng-GFP mouse was a gift from Andrew Groves (Baylor College of Medicine, Houston, TX). The Lfng-GFP mouse line is crossed with the ROSA26-DTA (diphtheria toxin subunit A) mouse line (stock #010527, The Jackson Laboratory; Wu et al., 2006) for at least 10 generations.

Immunofluorescence on frozen spinal cord tissues. Mice were anesthetized under isoflurane inhalation and perfused transcardially with 1× PBS, pH 7.4, followed by 4% paraformaldehyde (PFA). Spinal cords were dissected out and postfixed with 4% PFA overnight and then put in 20% sucrose for cryoprotection before being sectioned into 20 µm and attached to microscope slides (VistaVision, catalog #16004–406, VWR). Slides with spinal cord sections were washed with 1× PBS 5 min ×3, blocked with 10% goat or donkey serum in PBS with 0.3% Triton X-100, and incubated with primary antibodies in blocking solution overnight. The following primary antibodies were used at the following concentrations: chicken anti-GFP (1:1000; catalog #ab13970, Abcam); isolectin GS-IB4 (isolectin B4) Alexa Fluor 647 conjugate (1:100; catalog #I32450, Thermo Fisher Scientific); rabbit anti-neurokinin 1 receptor (NK1R; 1:500; catalog #S8305, Sigma-Aldrich); mouse anti-glutamic acid decarboxylase 67 (GAD67) antibody (1:500; catalog #MAB5406, Millipore); guinea pig anti-vesicular glutamate transporter 1 (VGluT1) antibody (1:1000; catalog #AB5905, Sigma-Aldrich); guinea pig anti-VGluT2 antibody (1:5000; catalog #AB2251, Millipore); rabbit anti-nuclear factor I-A (NFIA; 1:500; catalog #HPA006111, Sigma-Aldrich); rabbit anti-Olig2 (oligodendrocyte transcription factor 2; 1:500; catalog #ab42453, Abcam); goat anti-Sox9 (1:750; catalog #AF3075, R&D Systems); mouse anti-NeuN (neuronal-specific nuclear protein) 1:1000; catalog #MAB377, Millipore); goat anti-aldolase C (AldoC) antibody (1:500; catalog #sc-271593, Santa Cruz Biotechnology); mouse anti-GFAP (1:1000; catalog #MAB360, EMD Millipore); rabbit anti-S100 (1:1000; catalog #Z 0311, DakoCytomation); rabbit anti-β catenin antibody (1:500; catalog #ab6302, Abcam); rabbit anti-Hes1 (1:100; catalog #ab71559, Abcam); guinea pig anti-vesicular GABA transporter (VGAT; 1:350; catalog #1310044, Synaptic Systems); mouse anti-gephyrin (1:600; catalog #147011, Synaptic Systems); and rabbit anti-PSD-95 (1:300; catalog #51–6900, Thermo Fisher Scientific). Sections were then incubated for 1 h with the following secondary antibodies: Alexa Fluor 488 goat anti-chicken (1:500; catalog #A11039, Thermo Fisher Scientific); Alexa Fluor 568 goat anti-rabbit (1:500; catalog #A10036, Thermo Fisher Scientific); Alexa Fluor 568 goat anti-mouse (1:500; catalog #A11004, Thermo Fisher Scientific); and Alexa Fluor 568 donkey anti-goat (1:500; catalog #A11057, Thermo Fisher Scientific). Fluorescent imaging was performed using Zeiss Imager M2 and Z1 fluorescence microscope equipped with a Zeiss AxioCam camera and AxioVision software.

Preparation of spinal cord slices. To prepare spinal cord slices, all animals were deeply anesthetized with isoflurane. After decapitation, the spinal cord was quickly excised and submerged in an ice-cold cutting solution containing the following (in mM): 130 NaCl, 24 NaHCO3, 1.25 NaH_2PO_4, 3.5 KCl, 1.5 CaCl2, 1.5 MgCl2, and 10 D(+)-glucose, pH 7.4. The whole solution was gassed with 95%O_2-5% CO_2. The dura mater, and ventral and dorsal roots were removed. The spinal cord was glued to an upright agar block and placed in a slicing chamber with ice-cold pre-oxygenated incubation solution. We cut 300-μm-thick spinal cord coronal slices (lumbar segments L1–L5) using a vibratome. The slices were transferred to an extracellular ACSF solution (in mM): 130 NaCl, 24 NaHCO3, 1.25 NaH_2PO_4, 3.5 KCl, 1.5 CaCl2, 1.5 MgCl2, and 10 D(+)-glucose, pH 7.4. Slices were incubated at room temperature for at least 1 h before recording before being transferred to a recording chamber that was continuously perfused with ASCF solution (flow rate, 2 ml/min). The slice chamber was mounted on the stage of an upright microscope (Olympus) and viewed with a 60× water-immersion objective (numerical aperture = 0.90) with infrared differential interference contrast optics. For passive conductance measurement, astrocytes were patched with the following internal solution (in mM): 140 K-gluconate, 10 HEPES, 7 NaCl, and 2 MgATP, adjusted to pH 7.4 with CsOH and their membrane potentials were set at −60 mV. The voltage was injected from −120 to 120 mV for 1 s.

FACS sorting. We harvested and dissociated spinal cords using our previous protocols (John Lin et al., 2017). We used FACSAira III (BD) to sort dissociated astrocytes of different regions with a 100 μM nozzle. Approximately 50,000 GFP$^+$ astrocytes and 100,000 GFP$^-$ cells were collected per 1.5 ml tube, which contained 500 µl of Buffer RLT (catalog #79216, Qiagen) with 1% β-mercaptoethanol. In the end, each sample was vortexed and rapidly frozen on dry ice.

Total RNA extraction, library preparation, and sequencing. RNA was extracted from pelleted cells using the RNeasy Micro Kit (catalog #74004, QIAGEN). RNA integrity ≥8.0 was confirmed using the High Sensitivity RNA Analysis Kit [catalog #DNF-472–0500, Agilent (formerly AATI)] on a 12-capillary fragment analyzer. Illumina sequencing

libraries with 8 bp single indices were constructed from 10 ng of total RNA using the Trio RNA-Seq System (catalog #0507–96, NuGEN). We validated resulting libraries using the Standard Sensitivity NGS Fragment Analysis Kit [catalog #DNF-473–0500, Agilent (formerly AATI)] on a 12-capillary fragment analyzer. Equal concentrations (2 nM) of libraries were pooled and subjected to paired-end (2×75) sequencing of ~40 million reads per sample using the High Output v2 kit (catalog #FC-404–2002, Illumina) on a NextSeq550 following the manufacturer instructions.

Statistical analysis and bioinformatics data processing. We downloaded sequencing files from each flow cell lane and merged the resulting fastq files. Quality control was performed using fastQC (version 0.10.1) and MultiQC (version 0.9). Reads were mapped to the mouse genome mm10 assembly using STAR (version 2.5.0a). Bioconductor packages GenomicAlignments (version 1.16.0) and GenomicFeatures (version 1.32.2) were used to build count matrices. Normalization and differential expression were determined using DESeq2 (version 1.20.0) in R (version 3.5.2). RNA sequencing (RNA-Seq) data have been deposited on the National Institutes of Health GEO database (GSE186410). Genes were considered differentially expressed with an adjusted p value <0.05. We determined gene ontologies using Enrichr. Heatmap of expression values were plotted using the pheatmap R package.

Plasmids and adeno-associated virus generation. The Cre recombinase that is dependent on GFP (CRE-DOG) system consists of pAAV-EF1a-C-CreintG and pAAV-EF1a-N-CretrcintG (N-CRE), which were a gift from (Connie Cepko, Cambridge, Harvard University) (plasmid #69571, Addgene; http://n2t.net/addgene:69571; RRID:Addgene_69 571; and plasmid # 69570, Addgene; http://n2t.net/addgene:69570; RRID: Addgene_69 570, respectively; Tang et al., 2015). pAAV-EF1a-*N*-CreintG and pAAV-EF1a-C-CretrcintG (C-CRE) plasmids were used to generate AAV2/9 at a concentration of 3.85E12 and 5.26E12 genome copies/ml, respectively. All adeno-associated viruses (AAVs) were generated in the Optogenetics and Viral Vectors Core at the Jan and Dan Duncan Neurologic Research Institute.

Injection of the spinal cord. CRE-DOG, which combines the two AAVs, was injected into the dorsal white matter of the spinal cord of 8-week-old *Lfng-GFP; ROSA26-DTA* mice. Only one component of CRE-DOG was injected into the control group or control side. Morphologic, electrophysiological, and behavioral studies were conducted 4–5 weeks after the injection. Injections were performed on the L2-L3 segment of spinal cord. For the characterization of the efficiency of the viral injections, each mouse received one injection per side. For electrophysiological and behavioral characterization, each mouse received four injections on L2 and L3 segment per side. Injection volume is 1 μl.

Confocal imaging, synaptic staining, and quantification. Glutamatergic and GABAergic synapses were quantified with the Synapse Counter plugin for ImageJ (https://github.com/SynPuCo/SynapseCounter). Fluorescent images were acquired using a laser-scanning confocal microscope (model LSM 880, Zeiss) with the 63× oil-immersion objective. Serial images at the z-axis were taken at an optical step of 1 µm and encompassing the whole 30 µm section across replicates ($n = 3$ mice). Default parameters for 1024×1024 pixel images are used for glutamatergic and GABAergic synapse quantification using VGluT1–PSD-95, VGluT2–PSD-95, and VGAT–gephyrin pairs, respectively, in coronal sections. The regions of interest are selected within 100 µm of the ablation margin (where there are less Lfng-GFP$^+$ astrocytes) and compared with its contralateral site.

Electrophysiological recordings of dorsal spinal cord neurons. Field excitatory postsynaptic potential was measured in layer III-IV by electrical stimulation in layer I-II spinal cord. Electrical stimulation was delivered (from 100 to 500 μA with 0.2 ms duration every 10 s) through a concentric bipolar electrode (FHC), and the recording pipette was filled with 1 M NaCl solution. Electrical signals were digitized and sampled at 50 μs intervals with Digidata 1550B data acquisition system (Molecular Devices) using pCLAMP 10.2 software. Data were filtered at 2 kHz.

Hot plate test. We heated the hot plate surface to a constant temperature of 55°C. We placed mice on the hot plate and measured the latency to hindpaw response with a lick, flick, or jump (whichever came first). We then immediately removed the mouse from the plate and returned it to its cage. When a mouse did not respond within 30 s, we terminated the test and removed the mouse to prevent tissue damage. Each animal was tested only once.

von Frey filament test. To determine responses to mechanical stimuli, we used Aesthesio von Frey Kit, Touch Test Sensory Evaluator, which consists of 20 filaments based on the Semmes Weinstein Monofilament Set for touch assessment. Mice were placed on a perforated platform in a transparent Plexiglas chamber and habituated in their individual chambers for 1 h before the test. The series of von Frey fibers (0.04–1 g) was applied through the wire mesh onto the plantar surface of both hindpaws in ascending order, starting with the finest fiber. The filament was held in place for 1–1.5 s, then removed. We applied each von Frey hair five times at 5 s intervals for each paw (left and right), and calculated the percentage of paw withdrawal responses to gentle von Frey filament stimulation (Woo et al., 2014).

Cotton swab test. We used a "puffed out" cotton swab such that the cotton head was more than three times the normal size and applied it to hindpaws. We performed a <1 s stroke along the plantar paw surface five times, alternating between paws with a 10 s interval between, and recorded the number of paw withdrawals.

Adhesive removal test. For adhesive removal test, the home cage of the mice was first placed in the testing room. The feeder bin from the cage is removed and the mice habituated the testing room and the cage without the feeder for 1 h. While in the home cage, the mouse was then restrained and a cut adhesive tape was placed on alternating hindpaws. When the mouse makes an attempt to contact the adhesive label or try to remove it, time is recorded. If the mouse does not contact the adhesive label within 5 min trial is ended and label is removed by the experimenter. All mice receive five trials, with 24 h between trials and hindpaw labeled is rotated by day. Trials where the label falls off or is not secure are not counted (Bouet et al., 2009).

Experimental design and statistical analysis. Statistical analysis was performed using GraphPad Prism 9. Comparisons of averages of the resting potential and the capacitance of the ventral and Lfng-GFP$^+$ astrocytes were performed with the two-tailed, unpaired Student's t test (see Fig. 2*U–W*). Two-way ANOVA for repeated measures with *post hoc* analysis of the Bonferroni's test was used to determine statistical significance in current–voltage relationship (*I–V*) curve, where current is measured after voltage injection (see Fig. 2*T*). Characterization of ablation and control sides performed by setting the region of interest to the same size in all slices using ImageJ. The significance of the quantification of Lfng-GFP$^+$ and Sox9$^+$ cells is assessed by two-way ANOVA with Bonferroni's test (see Fig. 5*L*,*M*). The significance of NeuN$^+$ cells and synaptic markers are assessed with two-tailed, paired Student's t test (see Figs. 5*P*, 6*G–I*). Field EPSP (fEPSP) offline analysis was conducted using Clampfit in addition to GraphPad Prism 9. We assessed the significance of data for comparison by two-way ANOVA with Bonferroni's test (see Fig. 7*C*). For behavioral experiments, hot plate, cotton swab, and adhesive removal assay significance was determined by unpaired Student's t test, while the von Frey assay was tested with two-way ANOVA with Bonferroni's test (see Fig. 7*D–G*). Data are presented as the mean ± SEM. Levels of statistical significance are indicated as follows: $^*p < 0.05$, $^{**}p < 0.01$, $^{***}p < 0.001$. Details of statistical tests, precise p, n, t, and F values for each experiment are provided in the appropriate figure legends.

Results

Lfng-GFP reporter mice mark a laminae-specific cell population of the spinal cord

Prior studies established that Notch signaling plays a role in astrocyte differentiation and function (Ge et al., 2002; Namihira et al., 2009; Shimada et al., 2011; Wilhelmsson et al., 2012; Martini et al., 2013; Lebkuechner et al., 2015; LeComte et al., 2015; Acaz-Fonseca et al., 2019). Recently, the Lfng-GFP BAC reporter mouse was shown to specifically mark neural stem cells of the dentate gyrus (Semerci et al., 2017). This observation prompted us to examine Lfng-GFP expression in the developing and adult spinal cord, where we performed immunostaining

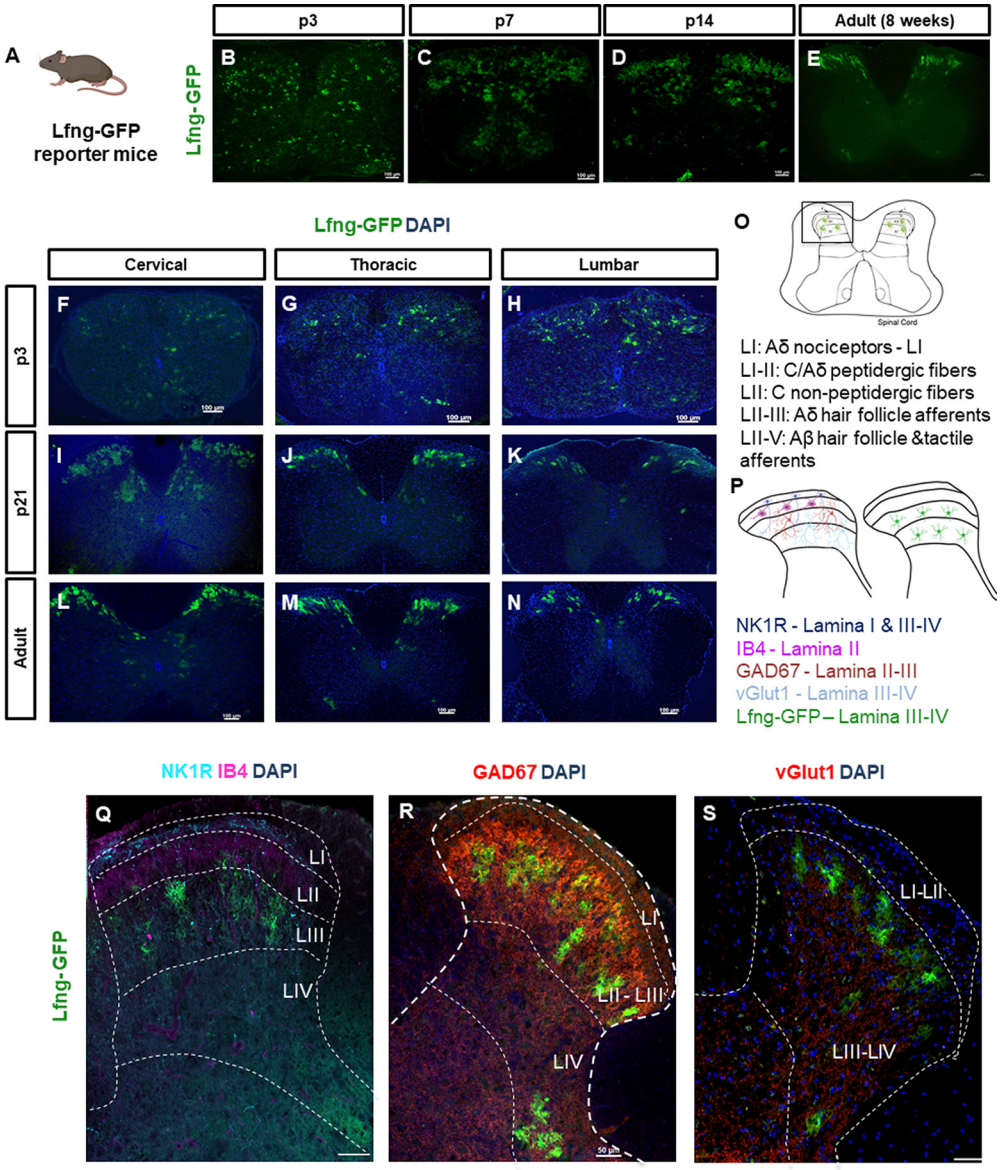

Figure 1. Lfng-GFP reporter mice mark a laminae-specific cell population in the dorsal spinal cord. ***A–E***, Spinal cord sections of Lfng-GFP reporter mice immunostained with GFP. At postnatal days 3, 7,14, and 21, GFP is expressed throughout the spinal cord. In the adult mice, Lfng-GFP expression is restricted to the dorsal horn of the spinal cord. Scale bar, 100 μm. ***F–N***, Lfng-GFP spinal cord is sectioned by segments: cervical, thoracic, and lumbar, and the dorsal-ventral expression pattern is consistent among the segments in p3 and p21, and in the adult. Scale bar, 100 μm. ***O***, ***P***, Diagram showing lamina markers in dorsal spinal cord and laminae where primary afferents terminate. ***Q***, IB4 marks lamina II, while neurons expressing NK1R are in laminae I, III, and IV. LFNG-GFP$^+$ cells are below lamina II. Scale bar, 50 μm. ***R***, ***S***, Immunohistochemistry for GAD67 to define the borders of Lamina III. VGluT1 is most abundant in laminae III and IV. Scale bar, 50 μm.

with GFP at postnatal days 3, 7,14, and 8 weeks in Lfng-GFP reporter mice. We found GFP was expressed throughout the spinal cord during early postnatal developmental stages; however, in adult mice, Lfng-GFP expression was restricted to the dorsal horn of the spinal cord (Fig. 1*B–E*). These expression patterns were uniformly present along with the cervical, thoracic, and lumbar segments of the spinal cord at p3, p21, and adult (Fig. 1*F–N*).

We next asked which laminae of the dorsal horn are occupied by Lfng-GFP$^+$ cells. Lamina II is marked by Bandeiraea simplicifolia IB4 (Wang et al., 1994) and NK1R labels neurons predominantly in lamina I and lamina III-IV (Sakamoto et al., 1999; Todd et al., 2000; Szabo et al., 2015). Coimmunostaining with NK1R, IB4, and GFP revealed that Lfng-GFP$^+$ cells colocalize with NK1R in lamina III and IV and do not colocalize with IB4, instead appearing to be localized in deeper laminae (Fig. 1*Q*). In parallel, we stained for GAD67 to define the borders of lamina III. Previous studies demonstrated that transgenic GAD67-GFP mice predominately labels neurons laminae I-III (Zeilhofer et al., 2009), and we found strong colocalization of Lfng-GFP with GAD67 (Fig. 1*R*). VGluT1 is most abundant in laminae III and IV (Alvarez et al., 2004) and can be used as defining the boundaries of lamina IV, and we found the colocalization of VGluT1 and Lfng-GFP in the dorsal boundaries (Fig. 1*S*). These studies indicate that Lfng-GFP reporter mice mark a specific cell population of the dorsal horn of the adult spinal cord in laminae III-IV, in which Aδ hair follicle afferents and Aβ hair follicle and tactile afferents terminate as well (Fig. 1*O*,*P*; Todd, 2010).

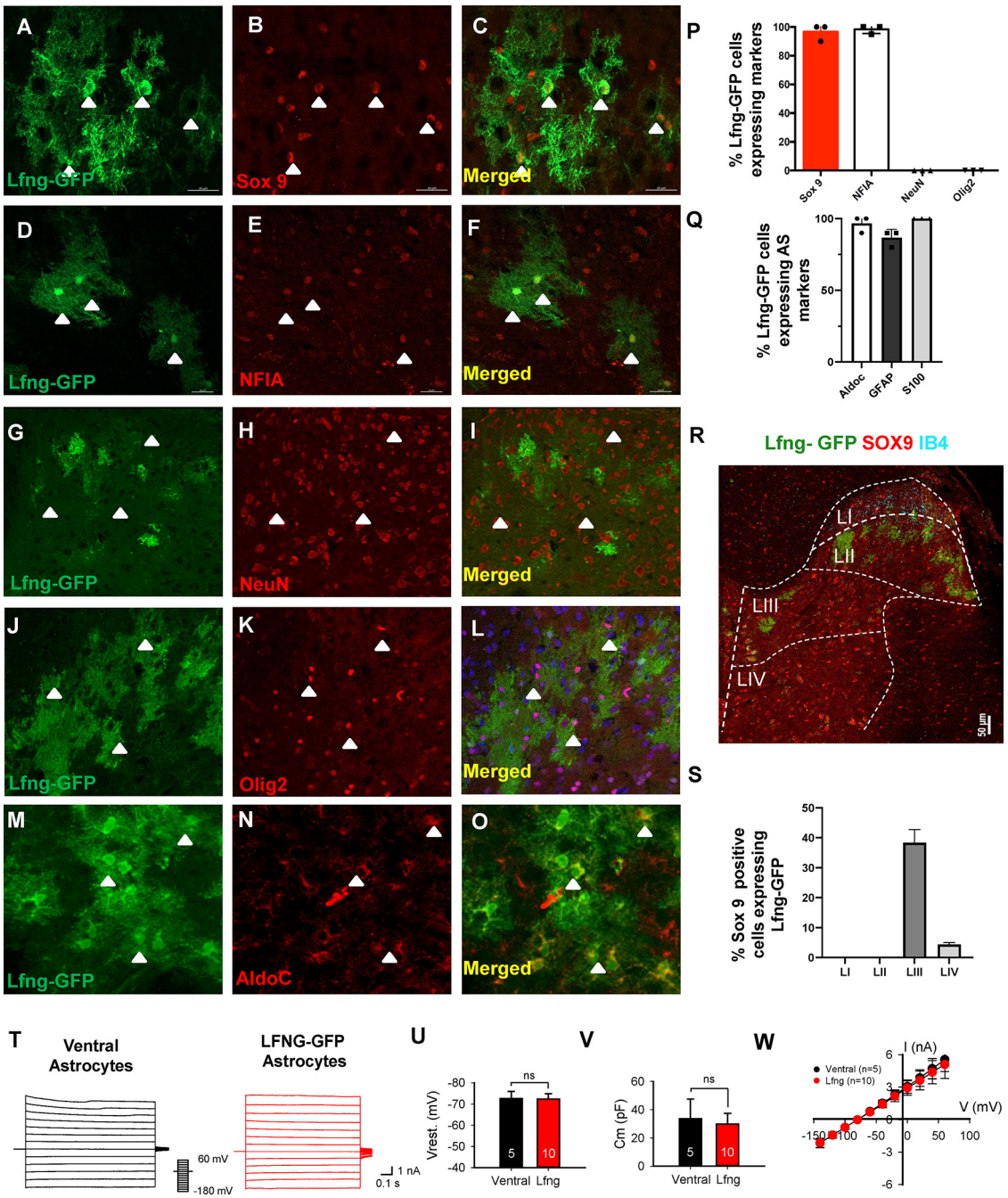

Figure 2. Lfng-GFP$^+$ cells exhibit molecular and physiological properties of astrocytes. ***A–F***, ***P***, Coexpression of NFIA, Sox9, and GFP. Lfng-GFP cells express astrocyte markers (SOX9: 98 ± 1.5%, $n = 40$ cells, nine slices from three mice; NFIA: 99 ± 1%, $n = 40$ cells, nine slices from three mice. Scale bar, 20 µm. ***G–L***, ***P***, Coexpression of NeuN and Olig2. Lfng-GFP cells do not express markers for neuronal and oligodendrocyte lineage (NeuN: 0.5%, $n = 40$ cells, nine slices from three mice; Olig2: 0.5%, $n = 40$ cells, nine slices from three mice). Scale bar, 20 µm. ***M–O***, ***Q***, Coexpression of AldoC and quantification of GFAP and S100B with GFP (AldoC: 97 ± 1.5% $n = 40$ cells, nine slices from three mice). Scale bar, 20 µm. ***R***, ***S***, Quantification of the percentage of Sox9 cells expressing Lfng-GFP. Scale bar, 50 µm. For lamina III, 38 ± 7.6%; for lamina IV, 4.3 ± 1.15%; $n = 3$ slices for three mice). ***T–V***, Whole-cell patch-clamp electrophysiology of astrocytes shows no significant differences in the membrane potential (ventral, −72.6 ± 3.4 mV; Lfng-GFP, −72.4 ± 2.4 mV; $t = 0.04673$, df = 13, $p = 0.9634$) and conductance (ventral, 33.6 ± 13.8 pF; Lfng-GFP; 29.96 ± 7.51 pF; $t = 0.2537$, df = 13, $p = 0.8037$) between two groups. Statistical comparisons were performed with the two-tailed, unpaired Student's t test (ventral astrocytes, $n = 5$; Lfng-GFP$^+$ astrocytes, $n = 10$). ***W***, Stepped voltage injections revealed no differences in I–V between Lfng-GFP$^+$ and ventral astrocytes (cell type: $F_{(1,13)} = 0.04$, $p = 0.8290$; group interaction: $F_{(13,169)} = 0.03$, $p > 0.9999$). Statistical comparisons were made using a two-way ANOVA (ventral astrocytes, $n = 5$; Lfng-GFP$^+$ astrocytes, $n = 10$). Data are presented as mean ± SEM (standard error of the mean). Levels of statistical significance are indicated as follows: * ($p < 0.05$), ** ($p < 0.01$), *** ($p < 0.001$), ns (not significant).

Lfng-GFP$^+$ cells have molecular and physiological properties of astrocytes

The morphologic characteristics of the Lfng-GFP$^+$ cells resembled protoplasmic astrocytes. Therefore, we next investigated which CNS lineage markers are coexpressed with Lfng-GFP. Examination of astrocyte markers Sox9 and NFIA revealed extensive coexpression with Lfng-GFP (SOX9: 98 ± 1.2%, $n = 40$ cells, nine slices from three mice; NFIA: 99 ± 1%, $n = 40$ cells, nine slices from three mice; Fig. 2*A–F*,*Q*). Further staining with NeuN (0.5 ± 0.2%, $n = 40$ cells, nine slices from three mice) or Olig2 (0.5 ± 0.3%, $n = 40$ cells, nine slices from three mice; Fig. 2*G–L*,*Q*) revealed nominal coexpression. These data indicate that

Lfng-GFP$^+$ cells are exclusively coexpressed with astrocyte markers. We corroborated these findings by staining with additional astrocyte markers, such as AldoC, GFAP, and S100β, and observed coexpression (AldoC: 97 $\pm$ 1.5%, $n = 40$ cells, nine slices from three mice; data not shown; Fig. 2*M–O*,*R*). Importantly, not all Sox9-expressing cells are positive for Lfng-GFP in laminae III and IV. We stained with IB4 to define these laminae and quantified percentage of Sox9 cells expressing Lfng-GFP, finding that 38% of lamina III astrocytes and 4.3% of lamina IV astrocytes express Lfng-GFP (Fig. 2*R*,*S*).

To evaluate whether the Lfng-GFP$^+$ cells possess the physiological properties of astrocytes, we performed whole-cell patch-clamp recordings on Lfng-GFP$^+$ astrocytes and Aldh1l1-GFP$^+$ astrocytes from the ventral spinal cord (ventral astrocytes, $n = 5$; Lfng-GFP$^+$ astrocytes, $n = 10$ cells from a total of three mice from each group). We did not find a significant difference in the membrane potential (unpaired Student's t test; ventral, -72.6 ± 3.4 mV; Lfng-GFP, -72.4 ± 2.4 mV; $t = 0.04673$, df = 13, $p = 0.9634$) and conductance (unpaired Student's t test; ventral, 33.6 ± 13.8 pF; Lfng-GFP, 29.96 ± 7.51 pF; $t = 0.2537$, df = 13, $p = 0.8037$) of both astrocyte groups. Stepped voltage injections revealed no differences in the I–V between Lfng-GFP$^+$ and ventral astrocytes (two-way ANOVA; cell type: $F_{(1,13)} = 0.04$, $p = 0.8290$; group interaction: $F_{(13,169)} = 0.03$, $p > 0.9999$; Fig. 2*S–W*). In conjunction with our cell lineage marker analysis, these observations indicate that Lfng-GFP$^+$ cells are astrocytes possessing similar membrane properties as ventral astrocytes.

Lfng-GFP$^+$ astrocytes exhibit unique molecular profiles

Having identified the Lfng-GFP$^+$ population as a lamina-specific astrocyte subpopulation, we asked whether it differs from other astrocytes in the spinal cord. We compared the molecular profiles of Lfng-GFP$^+$ astrocytes with astrocytes isolated from the aldehyde dehydrogenase family member L1 (Aldh1l1)-GFP reporter (Cahoy et al., 2008). We isolated Lfng-GFP$^+$ and Aldh1l1-GFP$^+$ astrocytes in addition to Lfng-GFP$^-$ and Aldh1l1-GFP$^-$ cells by FACS from 12-week-old adult spinal cords for mRNA-Seq analysis (Fig. 3*A*). We first verified that Lfng-GFP$^+$ and Aldh1l1-GFP$^+$ populations possessed molecular profiles consistent with astrocyte-specific signatures by comparing our dataset with a previously established list of astrocytic genes (John Lin et al., 2017; Fig. 3*B*). This analysis confirmed that Lfng-GFP$^+$ cells possess molecular profiles consistent with a pan-astrocytic signature and that we can successfully isolate these populations. Next, we sought to identify the molecular profile specific to Lfng-GFP$^+$ astrocytes. We analyzed differentially expressed genes (DEGs) by comparing Lfng-GFP$^+$ astrocytes with Aldh1l1-GFP$^+$ astrocytes by selected genes with a fold change >1.5 and $p < 0.05$ (Fig. 3*C*). These data indicate that Lfng-GFP$^+$ astrocytes exhibit unique molecular profiles that distinguish them from Ald1l1-GFP$^+$ astrocytes in the adult spinal cord. To further understand the unique molecular profiles of Lfng-GFP$^+$ astrocytes, we performed gene ontology (GO) analysis on the DEGs by comparing Lfng-GFP$^+$ astrocytes with Aldh1l1-GFP$^+$ astrocytes and Lfng-GFP$^+$ astrocytes with Lfng-GFP$^-$ cells. Major enriched processes in the GO analysis were Notch and Wnt signaling, and GABAergic and glutamatergic synaptic transmission (Fig. 3*D*,*E*). These studies indicate that Lfng-GFP$^+$ astrocytes have unique molecular signatures while also being enriched with astrocytic genes.

Among the GO terms and associated genes that highlighted Wnt signaling in Lfng-GFP$^+$ cells, we identified *Apcdd1*, *Axin 2*, and *Ctnnb1* (β-catenin; Fig. 4*A*). Wnts are a spinal cord morphogen that forms a dorsal-to-ventral concentration gradient (Megason and McMahon, 2002). In murine models of nerve injury, Wnt ligands are rapidly upregulated in dorsal horn neurons and astrocytes (Zhang et al., 2013; Liu et al., 2015). A recent study showed that an increase in Wnt ligands and β-catenin contributed to neuropathic pain by causing an increased expression of VGluT2 in the spinal cord (Zhang et al., 2020). Furthermore, the inhibition of Wnt ligands alleviated nociceptive sensitivity (Simonetti and Kuner, 2020). Notch signaling pathways *Lfng*, *Dll4*, *Notch3*, *Sox17*, *Jag1*, *Adam10*, and *Hes1* were also expressed in Lfng-GFP$^+$ astrocytes (Fig. 4*A*). Notch signaling pathway has a role in developing sensory organs, sensory processing, and plasticity (Dahlhaus et al., 2008; Lieber et al., 2011; Dias et al., 2014; Basch et al., 2016). In the dorsal spinal cord, Notch intracellular domain expression in the spinal cord dorsal horn is increased after spared nerve injury (SNI; Sun et al., 2012), in addition to an increase in mRNA levels of Hes1, which is a downstream target of Notch (Duan et al., 2021). Meanwhile, the inhibition of Notch decreased the pain response in the SNI model (Sun et al., 2012) and a diabetic peripheral neuropathic pain model (Chen et al., 2017). A recent study showed that a subpopulation of astrocytes was genetically defined by Hes5, a Notch effector, and had a critical role in mechanosensory behavior (Kohro et al., 2020).

Given the known roles of Wnt and Notch pathways in the spinal cord, we colabeled Lfng-GFP spinal cord sections with β-catenin and Hes1 antibodies. β-Catenin was predominantly expressed in the spinal cord dorsal horn. In addition, both β-catenin and Hes1 were enriched in Lfng-GFP$^+$ astrocytes (Fig. 4*B–G*). In summary, essential components of two signaling pathways associated with thermal and mechanical sensation are enriched in this subpopulation.

Combinatorial DTA and CRE-DOG system ablates Lfng-GFP$^+$ astrocytes

Our anatomic and molecular studies on the Lfng-GFP$^+$ astrocytes led us to hypothesize that Lfng-GFP$^+$ astrocytes contribute to sensory circuit activity in the dorsal spinal cord. To examine their prospective role in these processes, we next manipulated them by using the Lfng-GFP reporter to perturb their function. Previously, GFP lines have only been used to label cells, but recent technological developments allow us to manipulate these cells as well (Tang et al., 2013). A recently established system uses a split CRE-DOG to target and manipulate cells expressing GFP (Tang et al., 2015). CRE-DOG consists of two chimeric proteins with complementary split Cre fragments (N-CRE and C-CRE), each fused to a different GFP binding protein. When CRE-DOG is delivered via AAV, cells that specifically express GFP exhibit CRE activity (Fig. 5*A–C*).

We combined the CRE-DOG technology with a floxed mouse line, ROSA-DTA (Palmiter et al., 1987), that conditionally expresses DTA in the presence of Cre. These *Lfng-GFP; ROSA26-DTA* mice enabled us to ablate the Lfng-GFP$^+$ astrocytes with CRE-DOG injection (Fig. 5*A–C*). We injected virus into the L2 segment of the spinal cord when mice were 8 weeks old. N-CRE and C-CRE viruses were injected into the experimental side, while only the N-CRE virus was injected on the control side. Four weeks after injection, mice were perfused and stained with GFP and Sox9 antibodies. (Fig. 5*F–K*). We measured the efficiency of ablation by comparing Lfng-GFP$^+$ cells on experimental and control sides ($n = 3$ mice,

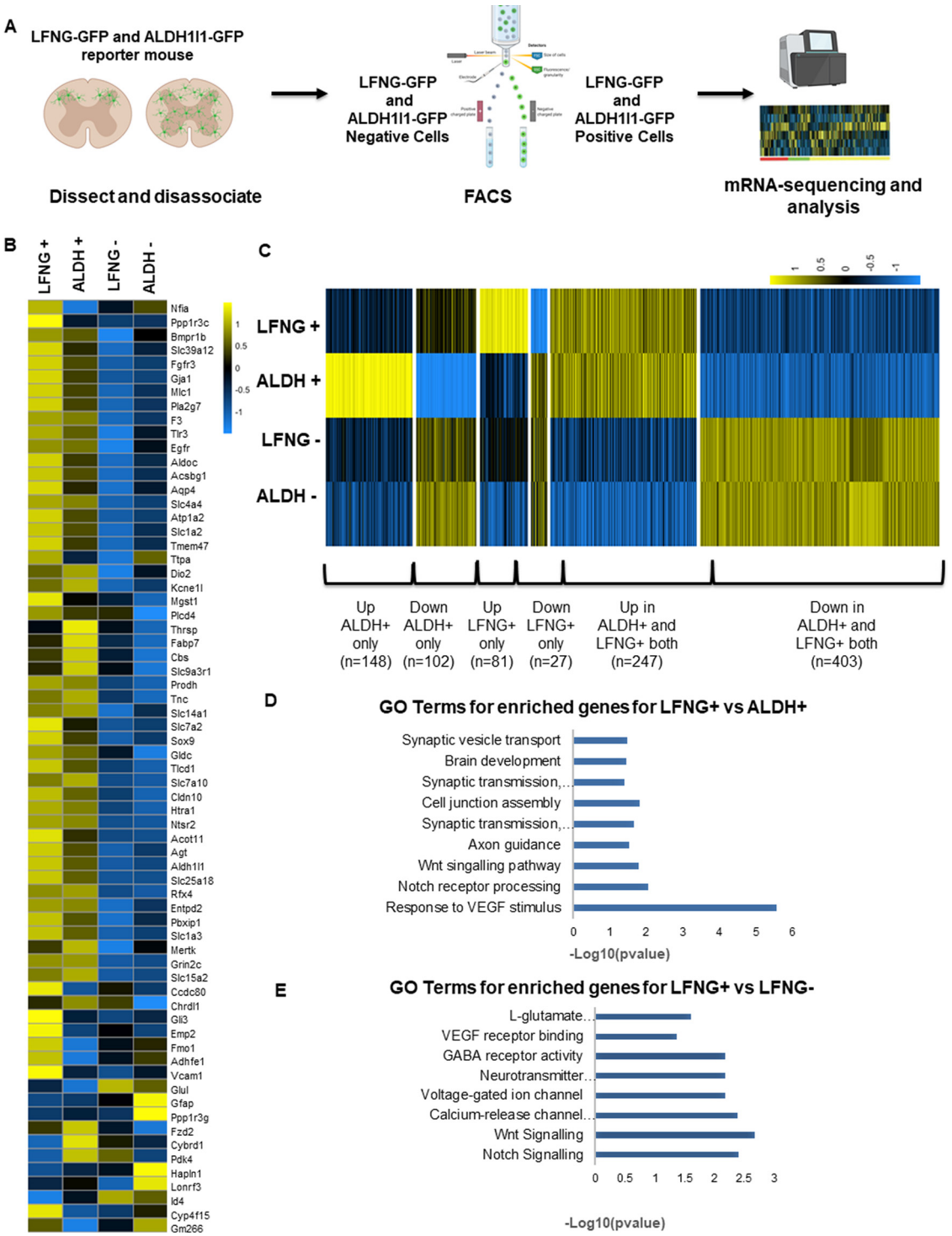

Figure 3. Lfng-GFP$^+$ astrocytes have a unique molecular signature. ***A***, Diagram showing dissection, disassociation, and collection of LFNG-GFP$^+$ and Aldhl1l-GFP$^+$ astrocytes for mRNA sequencing and analysis. ***B***, Comparing our dataset with astrocytic genes showed that Lfng-GFP$^+$ and Aldh1l1-GFP$^+$ populations possess molecular profiles consistent with astrocyte-specific signatures. ***C***, Analysis of differentially expressed genes in Lfng-GFP$^+$ astrocytes. Selected genes have a fold change >1.5 and $p < 0.05$. We found 148 genes enriched in only Aldh1l1-GFP$^+$ astrocytes and 81 genes only enriched in only LFNG-GFP$^+$ astrocytes, while 247 genes were enriched within both groups. ***D***, Examination of the GO terms was conducted in the comparison of LFNG-GFP$^+$ versus Aldhl1l-GFP$^+$ astrocytes. ***E***, Examination of the GO terms was conducted in the comparison of LFNG-GFP$^+$ astrocytes versus LFNG-GFP$^-$ cells.

three slices per distance from injection site). Viral ablation efficiency was highest in regions closest to the injection site and decreased with increasing distance from the injection site (two-way ANOVA; $n = 3$ sections from three mice; experimental group ablation vs nonablation: $F_{(1,4)} = 117.8$, $p = 0.0004$; group interaction: $F_{(2,8)} = 150.7$, $p < 0.0001$; 5 µm adjusted $p = 0.0007$, 75 µm adjusted $p = 0.0063$, 150 µm adjusted $p = 0.8409$; Fig. 5*L*). We also observed a decrease in the relative number of Sox9-expressing cells between the control and experimental groups at locations proximal to the injection site (two-way ANOVA; $n = 3$ sections from three mice; experimental group ablation vs nonablation: $F_{(1,4)} = 34.01$, $p = 0.0043$; group interaction: $F_{(2,8)} = 15.08$, $p = 0.0019$, 5 µm adjusted $p = 0.0058$, 75 µm adjusted $p = 0.0271$, 150 µm adjusted $p > 0.9999$; Fig. 5*M*). Finally, we assessed the number of neurons in these regions and did not

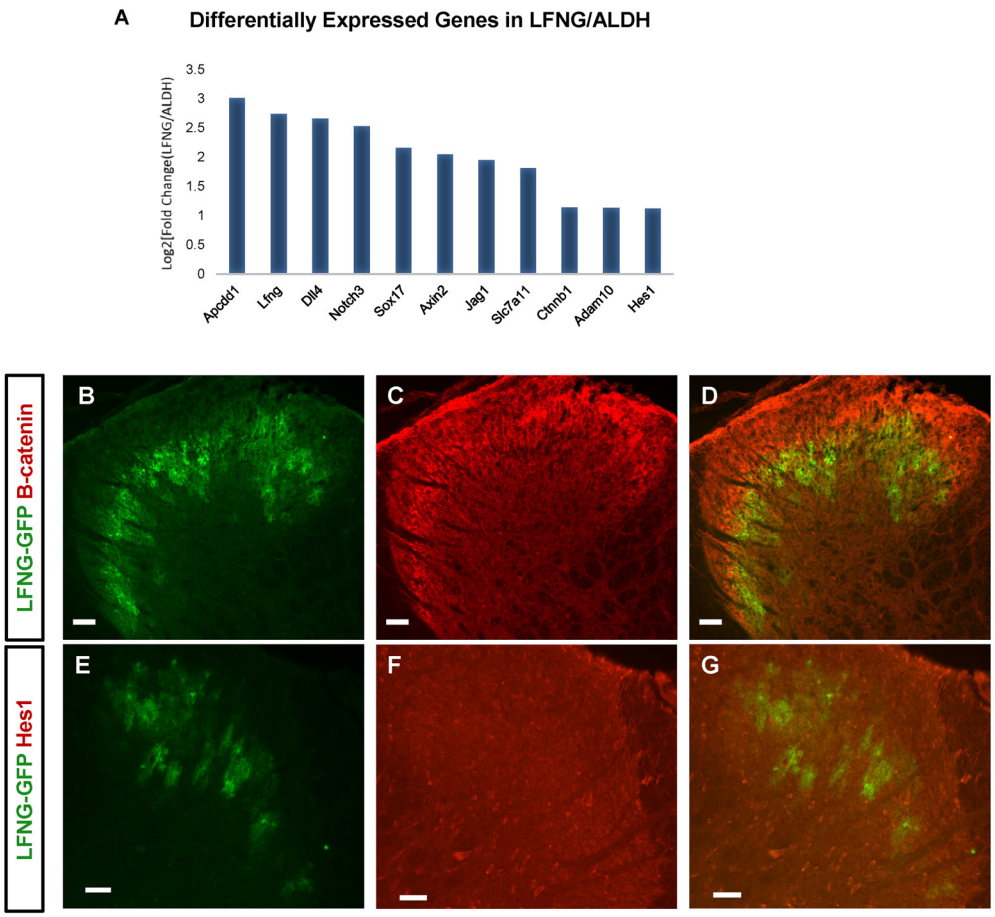

Figure 4. Lfng-GFP$^+$ astrocytes are enriched with Notch and Wnt signaling pathway genes. ***A***, Wnt-signaling genes *Apcdd1*, *Axin 2*, and *Ctnnb1* (β-catenin), and Notch signaling pathway genes *Lfng*, *Dll4*, *Notch3*, *Sox17*, *Jag1*, *Adam10*, and *Hes1* are enriched in Lfng-GFP$^+$ astrocytes. ***B–D***, β-Catenin is colocalized with Lfng-GFP$^+$ astrocytes. Scale bar, 20 μm. ***E–G***, Hes1 is colocalized with Lfng-GFP$^+$ astrocytes. Scale bar, 50 μm.

observe any significant changes in their numbers (unpaired Student's t test, $n = 3$ sections from three mice; control, 243 ± 6.6; CRE-DOG, 226 ± 4.8; $t = 1.462$, df = 2, $p = 0.2812$), suggesting that Lfng-GFP astrocytes are not required for neuronal survival and that our CRE-DOG targeting approach specifically impacted astrocytes (Fig. 5*N–P*). This characterization demonstrates that the CRE-DOG/DTA system can eliminate Lfng-GFP$^+$ astrocytes from the dorsal spinal cord and can be used to examine the role of these astrocytes in the dorsal spinal cord.

Ablation of Lfng-GFP$^+$ astrocytes impairs sensory circuit function

Using this model, we first evaluated how loss of Lfng-GFP$^+$ astrocytes impacted synapse numbers in the dorsal spinal cord. We first isolated experimental and control spinal cord from CRE-DOG-injected *Lfng-GFP; ROSA-DTA* mice and stained for synaptic markers in pairs of VGluT1/PSD-95, VGluT2/PSD-95, and VGAT/gephyrin (Fig. 6*A–F*) in laminae III and IV. We measured colocalization of these markers in experimental and control sides and found a significant decrease in glutamatergic synapses at the injection site but no change in the number of GABAergic synapses (paired Student's t test; $n = 3$ sections from three mice; VGluT1/PSD-95: control, 382.33 ± 13.691; CRE-DOG, 263.33 ± 22.303; $t = 13.11$, df = 2, $p = 0.0058$; VGluT2/PSD-95: control, 571.33 ± 12.347; CRE-DOG, 267.66 ± 35.983; $t = 12.21$, df = 2, $p = 0.0066$; VGAT/gephyrin: control, 429.33 ± 35.968; CRE-DOG, 422.23 ± 20.306; $t = 0.1573$, df = 2, $p = 0.8895$; Fig. 6*G–I*).

The decrease in the number of excitatory synapses led us to examine whether ablating Lfng-GFP$^+$ astrocytes also impacts circuit function in the dorsal spinal cord. In these experiments, the experimental group received two injections to both sides of the spinal cord, while control mice received only N-CRE injection to both sides at 8 weeks. Analysis occurred 4 weeks after injection. To test whether the ablation of Lfng-GFP$^+$ astrocytes affects synaptic transmission, we measured fEPSP amplitude from layer III-IV after applying electrical stimulation into the layer I-II spinal cord. We found a significant reduction in the input–out curve of fEPSP from Lfng-GFP$^+$ astrocyte-ablated spinal cords compared with controls (two-way ANOVA; $n = 10$ cells from each group with three mice per group; experimental group ablation vs nonablation: $F_{(1,18)} = 44.98$, $p < 0.0001$; group interaction: $F_{(5,90)} = 33.19$, $p < 0.0001$; Fig. 7*A–D*).

Having established that ablation of Lfng-GFP$^+$ astrocytes alters synaptic transmission of neurons in the dorsal spinal cord, we evaluated whether these changes have behavioral consequences. Given that VGluT1 synapses are associated with low-threshold mechanosensitive afferent terminals in the spinal cord and that VGluT2 synapses are associated with interneurons and nociceptive afferents, we examined sensory responses to thermal and mechanical stimuli in CRE-DOG-injected and control animals (Fig. 7*E–G*; Brumovsky, 2013). The CRE-DOG-injected group demonstrated similar sensitivity to controls in the hot plate

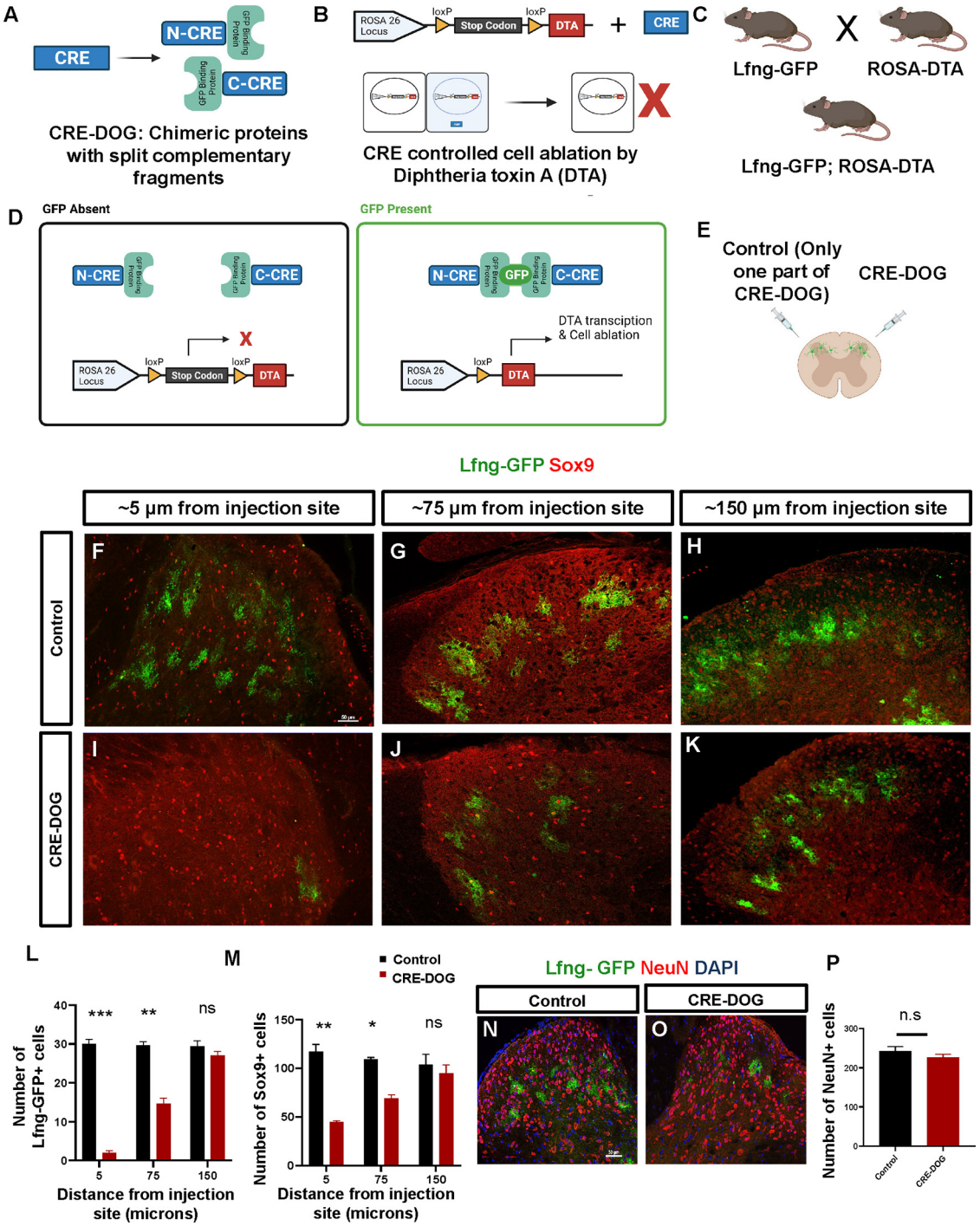

Figure 5. CRE-DOG and DTA mediated ablation of Lfng-GFP$^+$ astrocytes. ***A***, ***B***, Diagram explaining CRE-DOG and DTA. The CRE-DOG system uses two split fragments of Cre recombinase that unite as a functional Cre molecule only in the presence of GFP. Cre-controlled cell ablation occurs cell autonomously. ***C***, ***D***, Diagram showing mouse crosses and injection scheme. An Lfng-GFP mouse was crossed with a ROSA26-DTA mouse to generate a *Lfng-GFP; ROSA26-DTA* mouse. Cell ablation because of DTA expression is seen only in cells expressing GFP. ***E***, Diagram showing control and CRE-DOG injection sides. Only one component of the CRE-DOG system injected to control side. Contralateral side had both components of the CRE-DOG system. ***F–H***, Control injection side of the *Lfng-GFP; ROSA26-DTA* mouse. Coexpression GFP and Sox9. Lfng-GFP$^+$ astrocytes are present. Scale bar, 50 µm. ***I–K***, CRE-DOG injection side of *Lfng-GFP; ROSA26-DTA* mouse. Lfng-GFP$^+$ astrocytes are ablated. Scale bar, 50 µm. ***L***, Quantification of the relative number of Lfng-GFP$^+$ astrocytes from the CRE-DOG side (ablation) compared with the control side ($n = 3$ sections from three mice; experimental group ablation vs nonablation: $F_{(1,14)} = 117.8$, $p = 0.0004$; group interaction: $F_{(2,8)} = 150.7$, $p < 0.0001$; 5 µm adjusted $p = 0.0007$, 75 µm adjusted $p = 0.0063$, 150 µm adjusted $p = 0.8409$). Statistical comparisons were performed with the two-way ANOVA with Bonferroni's multiple-comparison test. ***M***, Quantification of the relative number of astrocytes from the CRE-DOG side (ablation) compared with the control side. ($n = 3$ sections from three mice; experimental group ablation vs nonablation: $F_{(1,4)} = 34.01$, $p = 0.0043$; group interaction: $F_{(2,8)} = 15.08$, $p = 0.0019$, 5 µm adjusted $p = 0.0058$, 75 µm adjusted $p = 0.0271$, 150 µm adjusted $p > 0.9999$). Statistical comparisons were performed with two-way ANOVA with Bonferroni's multiple-comparison test. ***N–P***, NeuN staining of control and ablation sites to quantify neurons. Scale bar, 50 µm ($n = 3$ sections from three mice; control, 243 ± 6.6; CRE-DOG, 226 ± 4.8; $t = 1.462$, df = 2, $p = 0.2812$). Statistical comparisons made performed with the two-tailed, unpaired Student's t test. Data are presented as mean ± SEM (standard error of the mean). Levels of statistical significance are indicated as follows: * ($p < 0.05$), ** ($p < 0.01$), *** ($p < 0.001$), ns (not significant).

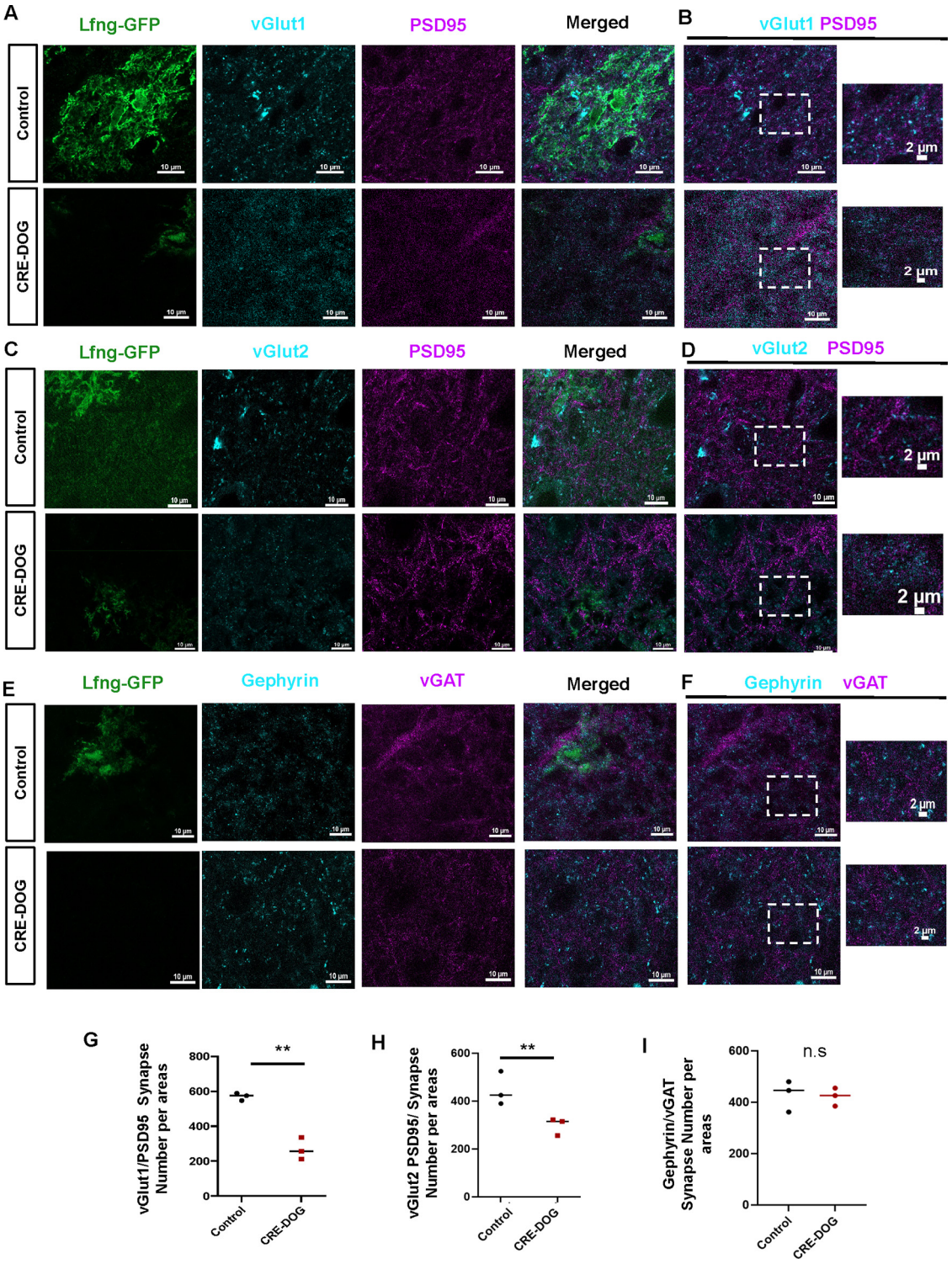

Figure 6. Ablation of Lfng-GFP^{+} astrocytes decreases glutamatergic synapses. ***A***, Glutamatergic synapse staining with VGluT1 and PSD-95 in control and ablation conditions. Scale bar, 10 µm. ***B***, Overlay of VGluT1 and PSD-95 staining. Scale bars: 10 µm; higher magnification, 2 µm in control and ablation conditions. ***C***, Glutamatergic synapse staining with VGluT2 and PSD-95 in control and ablation conditions. Scale bar, 10 µm. ***D***, Overlay of VGluT2 and PSD-95 staining. Scale bars: 10 µm; higher magnification, 2 µm in control and ablation conditions. ***E***, GABAergic synapse staining with gephyrin and VGAT in control and ablation conditions. Scale bar, 10 µm. ***F***, Overlay of gephyrin and VGAT. Scale bars: 10 µm; higher magnification, 2 µm in control and ablation conditions. ***G***, ***H***, Quantification of glutamatergic synapses using Synapse Counter on ImageJ (three slides per region; $n = 3$ mice, $n = 3$ sections from three mice; VGluT1/PSD-95: control, 382.33 ± 13.691; CRE-DOG, 263.33 ± 22.303; $t = 13.11$, df = 2, $p = 0.0058$; vGLUT2/PSD-95: control, 571.33 ± 12.347; CRE-DOG, 267.66 ± 35.983; $t = 12.21$, df = 2, $p = 0.0066$). Statistical comparisons were performed with the two-tailed, paired Student's *t* test. ***I***, Quantification of GABAergic synapse synapses using Synapse Counter on ImageJ (three slides per region; $n = 3$ mice; control, 429.33 ± 35.968; CRE-DOG, 422 ± 20.306; $t = 0.1573$, df = 2, $p = 0.8895$). Statistical comparisons were made performed with the two-tailed, paired Student's *t* test. Data are presented as mean ± SEM (standard error of the mean). Levels of statistical significance are indicated as follows: * ($p < 0.05$), ** ($p < 0.01$), *** ($p < 0.001$), ns (not significant).

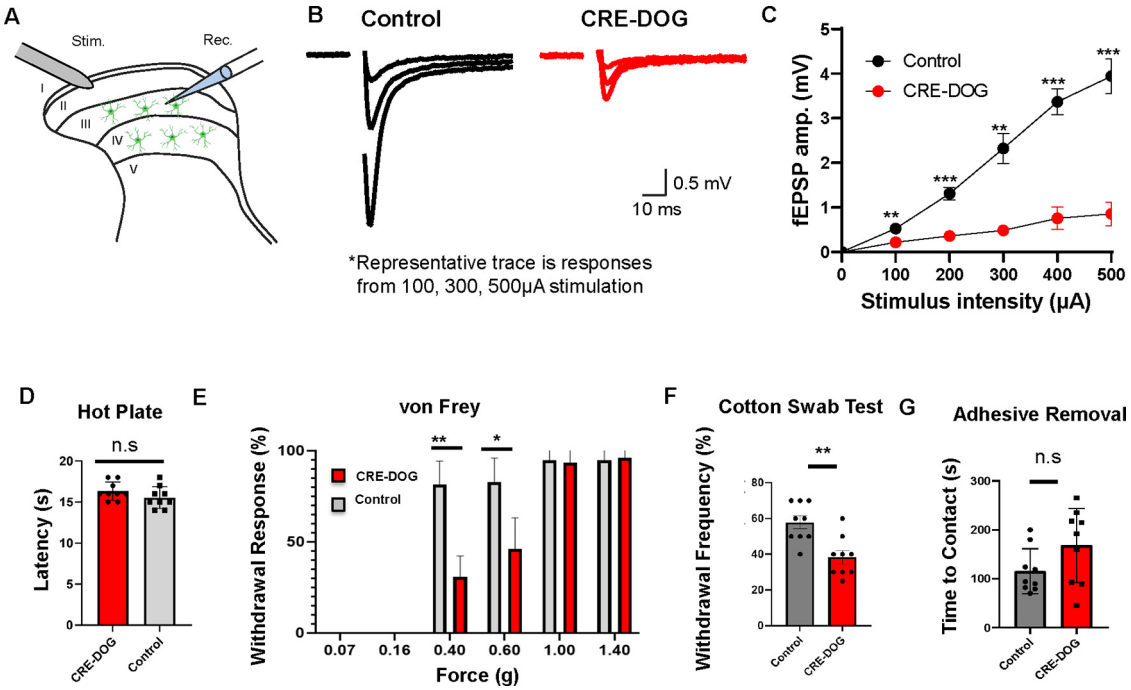

Figure 7. Ablation of Lfng-GFP$^+$ astrocytes impairs dorsal spinal cord circuit activity. ***A***, Diagram explaining measuring of fEPSP amplitude from layer III-IV after applying electrical stimulation into layer I-II spinal cord. ***B***, ***C***, Amplitude of fEPSP in control and CRE-DOG-injected *Lfng-GFP; ROSA26-DTA* mouse. In the CRE-DOG group, there is a significant reduction in controls (ablation vs nonablation: $F_{(1,18)} = 44.98$, $p < 0.0001$; group interaction: $F_{(5,90)} = 33.19$, $p < 0.0001$) in the input–out curve. Statistical comparisons were made performed with the two-way ANOVA with Bonferroni's multiple-comparison test ($n = 10$ cells from each group with three mice per group). ***D***, Both groups showed similar latency in hot plate test. (The CRE-DOG injected group demonstrated similar sensitivity to controls in the hot plate assay ($n = 9$ mice/ group; CRE-DOG, 16.333 ± 0.373; CRE-DOG, 15.556 ± 1.444; $t = 1.341$, df = 16, $p = 0.1987$). Statistical comparisons were performed with unpaired Student's t test. ***E***, Ablation of Lfng-GFP$^+$ astrocytes diminishes light touch sensitivity at 0.4 and 0.6 × g forces ($n = 15$ mice/group; experimental group ablation vs nonablation: $F_{(1,14)} = 106.4$, $p < 0.0001$; group interaction: $F_{(5,70)} = 53.32$, $p < 0.0001$). Statistical comparisons were performed with the two-way ANOVA with Bonferroni's multiple-comparison test. ***F***, Ablation group showed reduced paw withdrawal frequency in the cotton swab test ($n = 9$ mice/group; control, 57.78 ± 3.643; CRE-DOG, 38.33 ± 3.727; $t = 3.731$, df = 16, $p = 0.0018$). Statistical comparisons were made performed with unpaired Student's t test. ***G***, Both groups showed similar time to contact to adhesive label ($n = 9$ mice/group; control, 117.333 ± 15.376; CRE-DOG, 168.00 ± 25.343; $t = 1.777$, df = 16, $p = 0.0946$). Statistical comparisons were performed with unpaired Student's t test. Data are presented as mean ± SEM (standard error of the mean). Levels of statistical significance are indicated as follows: * ($p < 0.05$), ** ($p < 0.01$), *** ($p < 0.001$), ns (not significant).

assay (unpaired Student's t test; $n = 9$ mice/group; CRE-DOG, 16.333 ± 0.373; CRE-DOG, 15.556 ± 1.444; $t = 1.341$, df = 16, $p = 0.1987$; Fig. 7*D*), while the adhesive removal assay revealed a nonsignificant trend toward increased time to contact (unpaired Student's t test; $n = 9$ mice/group; control, 117.333 ± 15.376; CRE-DOG, 168.00 ± 25.343; $t = 1.777$, df = 16, $p = 0.0946$; Fig. 7*G*). However, in the von Frey assay (two-way ANOVA; $n = 15$ mice/group; experimental group ablation vs nonablation: $F_{(1,14)} = 106.4$, $p < 0.0001$; group interaction: $F_{(5,70)} = 53.32$, $p < 0.0001$) and cotton swab test (unpaired Student's t test; $n = 9$ mice/group; control, 57.78 ± 3.643; CRE-DOG, 38.33 ± 3.727; $t = 3.731$, df = 16, $p = 0.0018$), the CRE-DOG-injected group demonstrated significantly increased touch threshold and reduced sensitivity, respectively (Fig. 7*E*,*F*). Together, these findings indicate that Lfng-GFP$^+$ astrocytes play a key role in maintaining circuit functions that contribute to mechanosensation in the dorsal spinal cord.

Discussion

Our study used the Lfng-GFP reporter mouse to identify a lamina-specific subpopulation of astrocytes in the adult spinal cord. We characterized GFP expression in these mice during postnatal developmental stages and in adults using anatomic and cell lineage markers. Molecular profiling studies on Lfng-GFP$^+$ astrocytes identified the Notch and Wnt pathways as enriched in this population in the adult spinal cord. Using combinatorial CRE-DOG and DTA systems, we ablated Lfng-GFP$^+$ astrocytes and observed physiological and behavioral alterations. Collectively, our studies show that the Lfng-GFP population of astrocytes contributes to the maintenance of sensory circuits in the dorsal spinal cord.

The nature of astrocyte heterogeneity has rapidly emerged as an area of research over the past few years (Khakh and Deneen, 2019). Our finding of lamina-specific astrocyte subpopulations in the dorsal spinal cord parallels prior studies that identified diverse astrocyte subpopulations in the developing ventral spinal cord (Hochstim et al., 2008). Characterizing spinal cord astrocytes by their anatomic location has allowed for a deeper understanding of their functions, with prior studies revealing that dorsal astrocytes contribute to nociception (Nam et al., 2016; Kohro et al., 2020), while ventral astrocytes contribute to motor circuits (Molofsky et al., 2014). This notion of local or intraregional heterogeneity is also present in the adult brain, where several studies have identified molecularly distinct subpopulations of astrocytes within defined brain regions (John Lin et al., 2017; Batiuk et al., 2020; Bayraktar et al., 2020). Subsets of these subpopulations were shown to differentially influence synaptogenesis, indicating a level of functional diversity as well, though the precise anatomic location of these subpopulations with these regions remains poorly defined (John Lin et al., 2017). In addition to local heterogeneity, astrocytes also exhibit inter-regional heterogeneity across diverse brain regions (Chai et al., 2017; Morel et al., 2017; Lozzi et al., 2020). For instance, astrocytes from the

hippocampus and striatum exhibit differences in their potassium ion currents and calcium activity (Chai et al., 2017). In a parallel study, astrocytes in major cortical and subcortical brain areas were shown to have region-specific gene expression patterns; notably, astrocytes from cortical and subcortical regions had enhanced synapse formation with region-matched neurons (Morel et al., 2017).

In addition to distinct interactions with neurons, spinal cord astrocytes also exhibit unique physiological properties. A recent study demonstrated that while astrocytes in lamina I have faster coupling speed, higher responsiveness to potassium channel blockage and higher expression of AQP4 than astrocytes in lamina III, their basal membrane properties are similar (Kronschläger et al., 2021). This prompted us to compare passive conductance, *I–V* curve, and resting membrane potential between Lfng-GFP$^+$ and ventral Lfng-GFP$^-$ astrocytes, where we found no differences between these populations. Together, these observations indicate that passive linearity of membrane potential is a core feature of astrocytes that does not differ between these astrocyte subpopulations in the dorsal spinal cord. While differential expression astrocyte markers and connectiveness via coupling may help to attune to the differing needs of neurons, alterations in passive conductance and resting membrane potential may hinder the overall network. Differences in coupling and marker expression likely reflect distinct neuronal inputs, and understanding how specific neuronal interactions shape astrocytic properties is an area of active investigation.

Given the broad physiological roles of astrocytes, examining their cellular and functional heterogeneity requires an extensive set of selective tools. To characterize their anatomic, molecular, and physiological properties, several recent studies used Aldh1l1-GFP reporter mice or astrocyte-specific nuclear marker Sox9 to label astrocytes, genetic targeting with tamoxifen-inducible lines, and GFAP-driven viral tools to manipulate astrocyte activity (Shigetomi et al., 2016; Srinivasan et al., 2016; Khakh and Deneen, 2019; Yu et al., 2020). Here, we used a novel approach with Lfng-GFP reporter mice that labels a lamina-specific astrocyte subpopulation in the dorsal horn of the spinal cord. While the Lfng-GFP mouse allowed us to label these astrocytes, we required the CRE-DOG viral approach in combination with Cre-dependent expression of DTA to ablate them. CRE-DOG consists of two split fragments of Cre recombinase that form a functional Cre molecule only in the presence of GFP (Tang et al., 2015). Our study complements recent work that used designer receptors exclusively activated by designer drugs (DREADD)-based manipulations to define an astrocyte subpopulation in the spinal cord dorsal horn that contributes to mechanosensitivity (Kohro et al., 2020). These studies are based on the supposition that DREADD-based manipulations increase Ca^{2+} activity, thus increasing astrocyte activity and enhancing mechanosensitivity. In our studies, we eliminated astrocytes in the dorsal horn and found decreased circuit function and touch responses. Put together, these studies highlight the critical interplay between astrocytes and neurons in the processing of sensory information in the dorsal spinal cord.

We used an array of methods to elucidate the molecular and functional properties of a newly identified subpopulation of astrocytes in the dorsal spinal cord. Specifically, we complemented our loss-of-function manipulations with molecular profiling of Lfng-GFP$^+$ astrocytes and found that GFP$^+$ astrocytes are enriched in Notch, Wnt, and VEGF signaling pathway ligands, receptors, and modifiers. Critically, there is emerging evidence that the Wnt pathway plays a role in nociception by regulating sensory neuron excitability (Shi et al., 2012; Zhang et al., 2013, 2020; Itokazu et al., 2014; Liu et al., 2015). Moreover, inhibition of the Notch signaling pathway significantly increased the threshold to responding to thermal and mechanosensory stimuli in an SNI model (Sun et al., 2012), highlighting possible roles for these pathways in astrocyte–neuron communication in Lfng-GFP$^+$ astrocytes. Our ablation of a specific subpopulation of astrocytes enriched in components of the Notch pathway is unlikely to recapitulate all the sensory-processing effects observed with broader manipulations of Notch signaling that impact both neurons and astrocytes. Indeed, we observed specific defects in mechanosensation, but not in thermosensation (Fig. 7*D–G*). Nevertheless, it is quite striking that the ablation of a small, yet specific subset of astrocytes impacts circuit function, which further highlights the important role of astrocytes in sensory processing (Ung et al., 2021). The spinal cord dorsal horn is a complex center for integration of sensory information such as pain, itch, cold, warmth, and touch (Braz et al., 2014). Previous studies used intersectional genetic strategies to mark, ablate, and manipulate defined neuron subpopulations, which led to the conclusion that superficial laminae relay noxious information, while deeper laminae relay non-noxious information (Duan et al., 2014; Cheng et al., 2017). In our study, ablation of Lfng-GFP$^+$ astrocytes significantly reduced glutamatergic synapse markers and the input–out curve of fEPSP amplitude from layer III-IV after applying electrical stimulation. Next, we examined the behavioral consequences of these changes. We compared sensory information integration in CRE-DOG-ablated and control spinal cords using the following four well established behavioral assays: hot plate, von Frey, cotton swab, and adhesive removal tests. While the CRE-DOG-injected ablated group did not reveal significant differences in thermal sensations and adhesive removal test, we observed significantly reduced responses to low-threshold mechanical stimuli in von Frey and cotton swab tests.

One reason for this selective behavioral response may be that Lfng-GFP$^+$ astrocytes reside in laminae III-IV, which are innervated with afferents sensing light touch. The effect of ablation thus may not affect more superficial laminae, as these astrocytes only tile an area responsible for low-threshold mechanical stimuli. However, this observation raises the questions of whether regulation of mechanosensation by these astrocytes is because of their anatomic location, and whether if these astrocytes were located in more superficial laminae, would we see an effect on thermal nociception.

In summary, we used a variety of viral and mouse tools to identify a unique subpopulation of spinal cord astrocytes that has a role in the maintenance of synapses and circuit function in the dorsal spinal cord. Our study, in conjunction with previous studies, demonstrates that understanding astrocyte diversity is essential to understanding circuit function in the CNS, and that achieving these goals will require developing new tools and intersectional targeting technologies.

References

Acaz-Fonseca E, Ortiz-Rodriguez A, Azcoitia I, Garcia-Segura LM, Arevalo MA (2019) Notch signaling in astrocytes mediates their morphological response to an inflammatory challenge. Cell Death Discov 5:85.

Allen NJ, Barres BA (2009) Neuroscience: glia—more than just brain glue. Nature 457:675–677.

Allen NJ, Eroglu C (2017) Cell biology of astrocyte-synapse interactions. Neuron 96:697–708.

Alvarez FJ, Villalba RM, Zerda R, Schneider SP (2004) Vesicular glutamate transporters in the spinal cord, with special reference to sensory primary afferent synapses. J Comp Neurol 472:257–280.

Basch ML, Brown RM, Jen H-I, Semerci F, Depreux F, Edlund R, Zhang H, Norton CR, Gridley T, Cole SE, Doetzlhofer A, Maletic-Savatic M, Segil N, Groves AK (2016) Fine-tuning of Notch signaling sets the boundary of the organ of Corti and establishes sensory cell fates. eLife 5:e19921.

Batiuk MY, Martirosyan A, Wahis J, de Vin F, Marneffe C, Kusserow C, Koeppen J, Viana JF, Oliveira JF, Voet T, Ponting CP, Belgard TG, Holt MG (2020) Identification of region-specific astrocyte subtypes at single cell resolution. Nat Commun 11:1220.

Bayraktar OA, Bartels T, Holmqvist S, Kleshchevnikov V, Martirosyan A, Polioudakis D, Ben Haim L, Young AMH, Batiuk MY, Prakash K, Brown A, Roberts K, Paredes MF, Kawaguchi R, Stockley JH, Sabeur K, Chang SM, Huang E, Hutchinson P, Ullian EM, et al. (2020) Astrocyte layers in the mammalian cerebral cortex revealed by a single-cell in situ transcriptomic map. Nat Neurosci 23:500–509.

Ben Haim L, Rowitch DH (2017) Functional diversity of astrocytes in neural circuit regulation. Nat Rev Neurosci 18:31–41.

Bouet V, Boulouard M, Toutain J, Divoux D, Bernaudin M, Schumann-Bard P, Freret T (2009) The adhesive removal test: a sensitive method to assess sensorimotor deficits in mice. Nat Protoc 4:1560–1564.

Braz J, Solorzano C, Wang X, Basbaum AI (2014) Transmitting pain and itch messages: a contemporary view of the spinal cord circuits that generate gate control. Neuron 82:522–536.

Brumovsky PR (2013) VGLUTs in peripheral neurons and the spinal cord: time for a review. ISRN Neurol 2013:829753.

Cahoy JD, Emery B, Kaushal A, Foo LC, Zamanian JL, Christopherson KS, Xing Y, Lubischer JL, Krieg PA, Krupenko SA, Thompson WJ, Barres BA (2008) A transcriptome database for astrocytes, neurons, and oligodendrocytes: a new resource for understanding brain development and function. J Neurosci 28:264–278.

Chai H, Diaz-Castro B, Shigetomi E, Monte E, Octeau JC, Yu X, Cohn W, Rajendran PS, Vondriska TM, Whitelegge JP, Coppola G, Khakh BS (2017) Neural circuit-specialized astrocytes: transcriptomic, proteomic, morphological, and functional evidence. Neuron 95:531–549.e9.

Chen T, Li H, Yin Y, Zhang Y, Liu Z, Liu H (2017) Interactions of Notch1 and TLR4 signaling pathways in DRG neurons of in vivo and in vitro models of diabetic neuropathy. Sci Rep 7:1–12.

Cheng L, Duan B, Huang T, Zhang Y, Chen Y, Britz O, Garcia-Campmany L, Ren X, Vong L, Lowell BB, Goulding M, Wang Y, Ma Q (2017) Identification of spinal circuits involved in touch-evoked dynamic mechanical pain. Nat Neurosci 20:804–814.

Dahlhaus M, Hermans JM, van Woerden LH, Saiepour MH, Nakazawa K, Mansvelder HD, Heimel JA, Levelt CN (2008) Notch1 signaling in pyramidal neurons regulates synaptic connectivity and experience-dependent modifications of acuity in the visual cortex. J Neurosci 28:10794–10802.

Dias BG, Goodman JV, Ahluwalia R, Easton AE, Andero R, Ressler KJ (2014) Amygdala-dependent fear memory consolidation via miR-34a and notch signaling. Neuron 83:906–918.

Duan B, Cheng L, Bourane S, Britz O, Padilla C, Garcia-Campmany L, Krashes M, Knowlton W, Velasquez T, Ren X, Ross SE, Lowell BB, Wang Y, Goulding M, Ma Q (2014) Identification of spinal circuits transmitting and gating mechanical pain. Cell 159:1417–1432.

Duan H, Shen F, Li L, Tu Z, Chen P, Chen P, Wang Z, Liang W, Wang Y (2021) Activation of the Notch signaling pathway in the anterior cingulate cortex is involved in the pathological process of neuropathic pain. Pain 162:263–274.

Gao YJ, Zhang L, Ji RR (2010) Spinal injection of TNF-α-activated astrocytes produces persistent pain symptom mechanical allodynia by releasing monocyte chemoattractant protein-1. Glia 58:1871–1880.

Ge W, Martinowich K, Wu X, He F, Miyamoto A, Fan G, Weinmaster G, Sun YE (2002) Notch signaling promotes astrogliogenesis via direct CSL-mediated glial gene activation. J Neurosci Res 69:848–860.

Hochstim C, Deneen B, Lukaszewicz A, Zhou Q, Anderson DJ (2008) Identification of positionally distinct astrocyte subtypes whose identities are specified by a homeodomain code. Cell 133:510–522.

Itokazu T, Hayano Y, Takahashi R, Yamashita T (2014) Involvement of Wnt/β-catenin signaling in the development of neuropathic pain. Neurosci Res 79:34–40.

Ji RR, Donnelly CR, Nedergaard M (2019) Astrocytes in chronic pain and itch. Nat Rev Neurosci 20:667–685.

John Lin C-C, Yu K, Hatcher A, Huang T-W, Lee HK, Carlson J, Weston MC, Chen F, Zhang Y, Zhu W, Mohila CA, Ahmed N, Patel AJ, Arenkiel BR, Noebels JL, Creighton CJ, Deneen B (2017) Identification of diverse astrocyte populations and their malignant analogs. Nat Neurosci 20:396–405.

Khakh BS, Deneen B (2019) The emerging nature of astrocyte diversity. Annu Rev Neurosci 42:187–207.

Khakh BS, Sofroniew MV (2015) Diversity of astrocyte functions and phenotypes in neural circuits. Nat Neurosci 18:942–952.

Kohro Y, Matsuda T, Yoshihara K, Kohno K, Koga K, Katsuragi R, Oka T, Tashima R, Muneta S, Yamane T, Okada S, Momokino K, Furusho A, Hamase K, Oti T, Sakamoto H, Hayashida K, Kobayashi R, Horii T, Hatada I, et al. (2020) Spinal astrocytes in superficial laminae gate brainstem descending control of mechanosensory hypersensitivity. Nat Neurosci 23:1376–1387.

Kronschläger MT, Siegert ASM, Resch FJ, Rajendran PS, Khakh BS, Sandkühler J (2021) Lamina-specific properties of spinal astrocytes. Glia 69:1749–1766.

Lebkuechner I, Wilhelmsson U, Möllerström E, Pekna M, Pekny M (2015) Heterogeneity of Notch signaling in astrocytes and the effects of GFAP and vimentin deficiency. J Neurochem 135:234–248.

LeBon L, Lee T. v, Sprinzak D, Jafar-Nejad H, Elowitz MB (2014) Fringe proteins modulate Notch-ligand cis and trans interactions to specify signaling states. eLife 3:e02950.

LeComte MD, Shimada IS, Sherwin C, Spees JL (2015) Notch1-STAT3-ETBR signaling axis controls reactive astrocyte proliferation after brain injury. Proc Natl Acad Sci U S A 112:8726–8731.

Lieber T, Kidd S, Struhl G (2011) DSL-notch signaling in the Drosophila brain in response to olfactory stimulation. Neuron 69:468–481.

Liu S, Liu YP, Huang ZJ, Zhang YK, Song AA, Ma PC, Song XJ (2015) Wnt/Ryk signaling contributes to neuropathic pain by regulating sensory neuron excitability and spinal synaptic plasticity in rats. Pain 156:2572–2584.

Lozzi B, Huang TW, Sardar D, Huang AYS, Deneen B (2020) Regionally distinct astrocytes display unique transcription factor profiles in the adult brain. Front Neurosci 14:61.

Martini S, Bernoth K, Main H, Ortega GDC, Lendahl U, Just U, Schwanbeck R (2013) A critical role for Sox9 in Notch-induced astrogliogenesis and stem cell maintenance. Stem Cells 31:741–751.

Megason SG, McMahon AP (2002) A mitogen gradient of dorsal midline Wnts organizes growth in the CNS. Development 129:2087–2098.

Molofsky AV, Deneen B (2015) Astrocyte development: a guide for the perplexed. GLIA 63:1320–1329.

Molofsky AV, Kelley KW, Tsai H-H, Redmond SA, Chang SM, Madireddy L, Chan JR, Baranzini SE, Ullian EM, Rowitch DH (2014) Astrocyte-encoded positional cues maintain sensorimotor circuit integrity. Nature 509:189–194.

Morel L, Chiang MSR, Higashimori H, Shoneye T, Iyer LK, Yelick J, Tai A, Yang Y (2017) Molecular and functional properties of regional astrocytes in the adult brain. J Neurosci 37:8706–8717.

Nam Y, Kim J-H, Kim J-H, Hwang S-H, Cho H-J, Correspondence KS, Jha MK, Jung JY, Lee M-G, Choi I-S, Jang I-S, Lim DG, Suk K (2016) Reversible induction of pain hypersensitivity following optogenetic stimulation of spinal astrocytes. Cell Rep 17:3049–3061.

Namihira M, Kohyama J, Semi K, Sanosaka T, Deneen B, Taga T, Nakashima K (2009) Committed neuronal precursors confer astrocytic potential on residual neural precursor cells. Dev Cell 16:245–255.

Palmiter RD, Behringer RR, Quaife CJ, Maxwell F, Maxwell IH, Brinster RL (1987) Cell lineage ablation in transgenic mice by cell-specific expression of a toxin gene. Cell 50:435–443.

Ramon y Cajal S (1897) Histology of the nervous system of man and vertebrates. New York: Oxford UP.

Sakamoto H, Spike RC, Todd AJ (1999) Neurons in laminae III and IV of the rat spinal cord with the neurokinin-1 receptor receive few contacts from unmyelinated primary afferents which do not contain substance P. Neuroscience 94:903–908.

Semerci F, Tin S, Choi W, Bajic A, Thakkar A, Encinas JM, Depreux F, Segil N, Groves AK, Maletic-Savatic M (2017) Lunatic fringe-mediated notch signaling regulates adult hippocampal neural stem cell maintenance. eLife 6:e24660.

Shi Y, Yuan S, Li B, Wang J, Carlton SM, Chung K, Chung JM, Tang SJ (2012) Regulation of Wnt signaling by nociceptive input in animal models. Mol Pain 8:47.

Shigetomi E, Patel S, Khakh BS (2016) Probing the complexities of astrocyte calcium signaling. Trends Cell Biol 26:300–312.

Shimada IS, Borders A, Aronshtam A, Spees JL (2011) Proliferating reactive astrocytes are regulated by notch-1 in the peri-infarct area after stroke. Stroke 42:3231–3237.

Simonetti M, Kuner R (2020) Spinal Wnt5a plays a key role in spinal dendritic spine remodeling in neuropathic and inflammatory pain models and in the proalgesic effects of peripheral Wnt3a. J Neurosci 40:6664–6677.

Srinivasan R, Lu T-Y, Chai H, Xu J, Huang BS, Golshani P, Coppola G, Khakh BS (2016) New transgenic mouse lines for selectively targeting astrocytes and studying calcium signals in astrocyte processes in situ and in vivo. Neuron 92:1181–1195.

Sun YY, Li L, Liu XH, Gu N, Dong HL, Xiong L (2012) The spinal notch signaling pathway plays a pivotal role in the development of neuropathic pain. Mol Brain 5:23.

Szabo NE, da Silva RV, Sotocinal SG, Zeilhofer HU, Mogil JS, Kania A (2015) Hoxb8 intersection defines a role for Lmx1b in excitatory dorsal horn neuron development, spinofugal connectivity, and nociception. J Neurosci 35:5233–5246.

Tang JCY, Szikra T, Kozorovitskiy Y, Teixiera M, Sabatini BL, Roska B, Cepko CL (2013) A nanobody-based system using fluorescent proteins as scaffolds for cell-specific gene manipulation. Cell 154:928–939.

Tang JCY, Rudolph S, Dhande OS, Abraira VE, Choi S, Lapan SW, Drew IR, Drokhlyansky E, Huberman AD, Regehr WG, Cepko CL (2015) Cell type–specific manipulation with GFP-dependent Cre recombinase. Nat Neurosci 18:1334–1341.

Todd AJ (2010) Neuronal circuitry for pain processing in the dorsal horn. Nat Rev Neurosci 11:823–836.

Todd AJ, McGill MM, Shehab SAS (2000) Neurokinin 1 receptor expression by neurons in laminae I, III and IV of the rat spinal dorsal horn that project to the brainstem. Eur J Neurosci 12:689–700.

Tsai H-H, Li H, Fuentealba LC, Molofsky AV, Taveira-Marques R, Zhuang H, Tenney A, Murnen AT, Fancy SPJ, Merkle F, Kessaris N, Alvarez-Buylla A, Richardson WD, Rowitch DH (2012) Regional astrocyte allocation regulates CNS synaptogenesis and repair. Science 337:358–362.

Tsuda M, Kohro Y, Yano T, Tsujikawa T, Kitano J, Tozaki-Saitoh H, Koyanagi S, Ohdo S, Ji RR, Salter MW, Inoue K (2011) JAK-STAT3 pathway regulates spinal astrocyte proliferation and neuropathic pain maintenance in rats. Brain 134:1127–1139.

Ung K, Huang TW, Lozzi B, Woo J, Hanson E, Pekarek B, Tepe B, Sardar D, Cheng YT, Liu G, Deneen B, Arenkiel BR (2021) Olfactory bulb astrocytes mediate sensory circuit processing through Sox9 in the mouse brain. Nat Commun 12:5230.

Wang H, Rivero-Melián C, Robertson B, Grant G (1994) transganglionic transport and binding of the isolectin B4 from Griffonia simplicifolia I in rat primary sensory neurons. Neuroscience 62:539–551.

Wilhelmsson U, Faiz M, de Pablo Y, Sjöqvist M, Andersson D, Widestrand Å, Potokar M, Stenovec M, Smith PLP, Shinjyo N, Pekny T, Zorec R, Ståhlberg A, Pekna M, Sahlgren C, Pekny M (2012) Astrocytes negatively regulate neurogenesis through the Jagged1-mediated notch pathway. Stem Cells 30:2320–2329.

Woo S-H, Ranade S, Weyer AD, Dubin AE, Baba Y, Qiu Z, Petrus M, Miyamoto T, Reddy K, Lumpkin EA, Stucky CL, Patapoutian A (2014) Piezo2 is required for Merkel cell mechanotransduction. Nature 509:622–626.

Wu S, Wu Y, Capecchi MR (2006) Motoneurons and oligodendrocytes are sequentially generated from neural stem cells but do not appear to share common lineage-restricted progenitors in vivo. Development 133:581–590.

Yu X, Nagai J, Khakh BS (2020) Improved tools to study astrocytes. Nat Rev Neurosci 21:121–138.

Zeilhofer HU, Witschi R, Johansson T (2009) Fast inhibitory transmission of pain in the spinal cord. In: Synaptic plasticity in pain (Malcangio M, eds), pp 49–66. New York: Springer.

Zhang YK, Huang ZJ, Liu S, Liu YP, Song AA, Song XJ (2013) WNT signaling underlies the pathogenesis of neuropathic pain in rodents. J Clin Invest 123:2268–2286.

Zhang ZL, Yu G, Peng J, Wang HB, Li YL, Liang XN, Su R, binGong ZH (2020) Wnt1/β-catenin signaling upregulates spinal VGLUT2 expression to control neuropathic pain in mice. Neuropharmacology 164:107869.